Supplementary Information

A survey of earth abundant metal oxides as oxygen evolution electrocatalysts in acidic media (pH < 1)

Jiahao Yu,[1,2] Stefano Giancola,[1] Bahareh Khezri,[1,2] David Nieto-Castro,[1] Jesús Redondo,[3,4] Frederik Schiller,[3,5] Sara Barja,[3,5,6] Maria Chiara Spadaro,[7] Jordi Arbiol,[7,8] Felipe A. Garcés-Pineda[1*] and José Ramón Galán-Mascarós[1,8*]

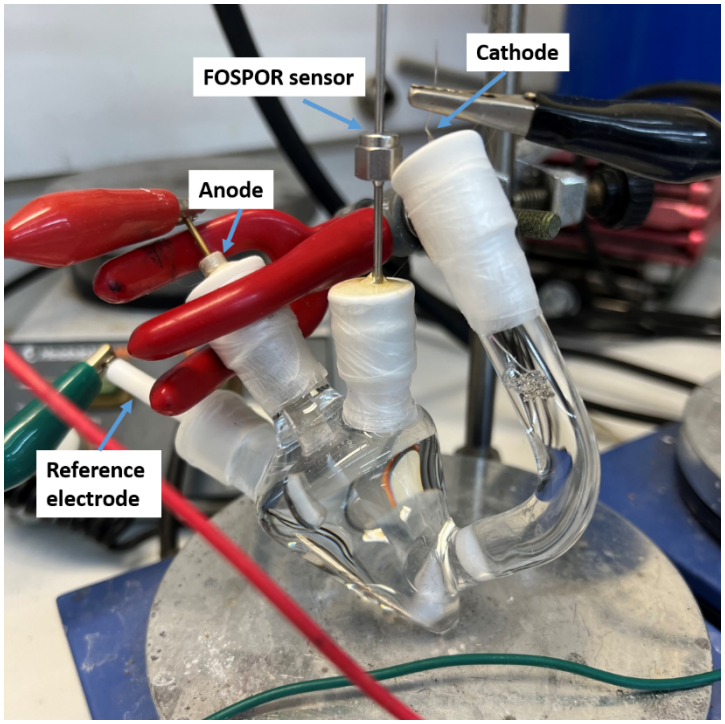

Figure S1. Setup for oxygen evolution measurement. It includes a personalized H-type cell containing the Mn_2O_3/GPO anode, Pt cathode and Ag/AgCl (3 M KCl) reference electrode connected to the potentiostat, the FOSPOR sensor connected to the anodic side headspace.

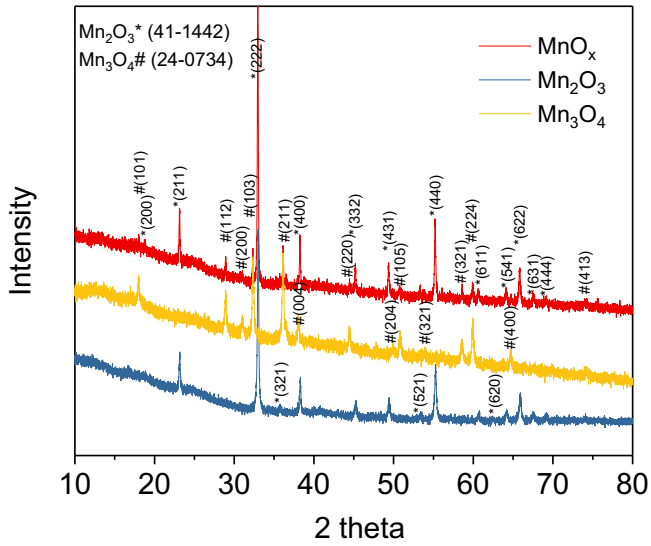

Figure S2. PXRD pattern for MnO_x, Mn_2O_3 and Mn_3O_4.

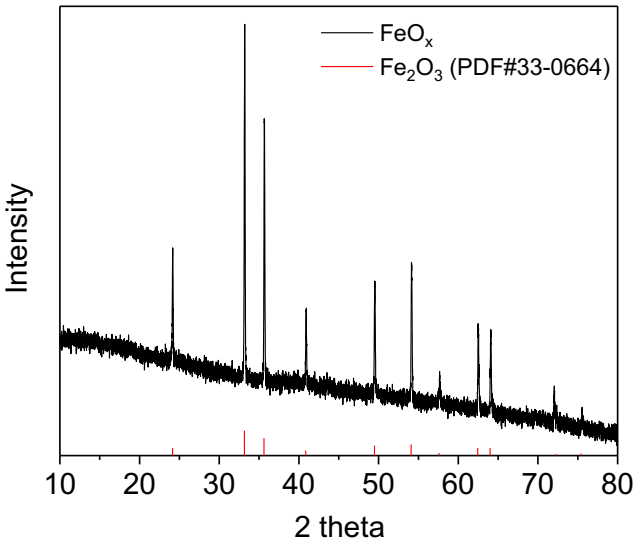

Figure S3. PXRD pattern for FeO_x.

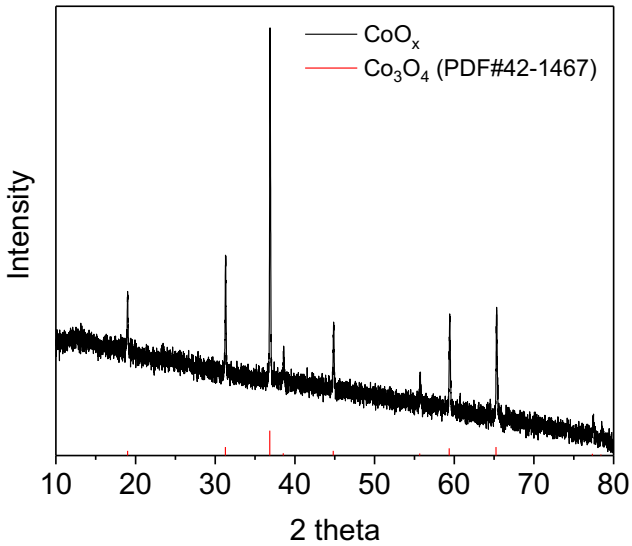

Figure S4. PXRD pattern for CoO_x.

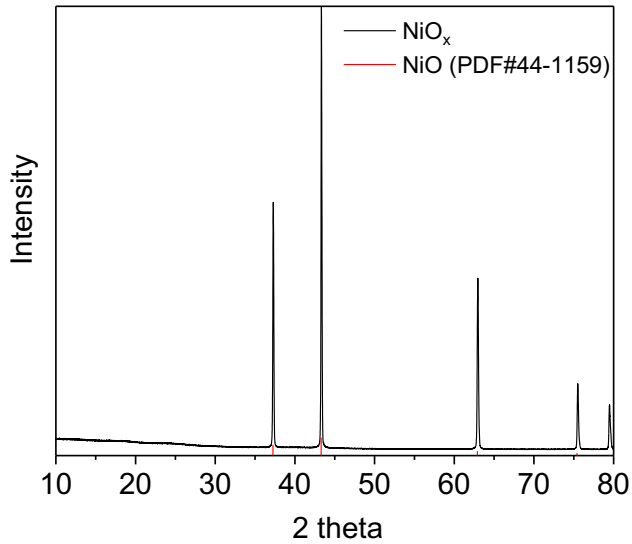

Figure S5. PXRD pattern for NiO_x.

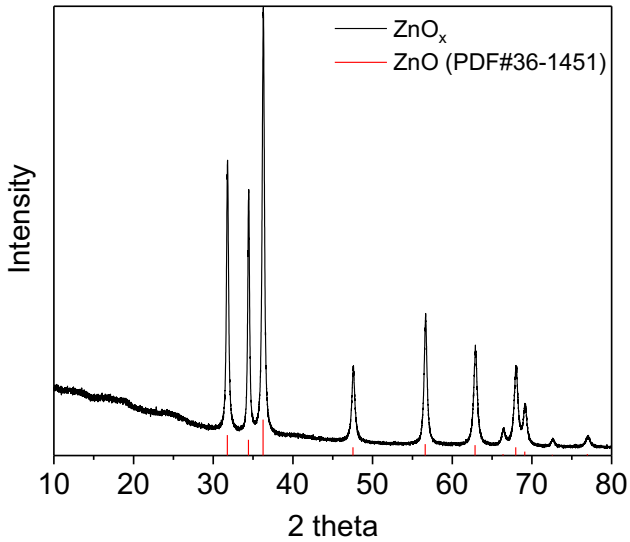

Figure S6. PXRD pattern for ZnO_x.

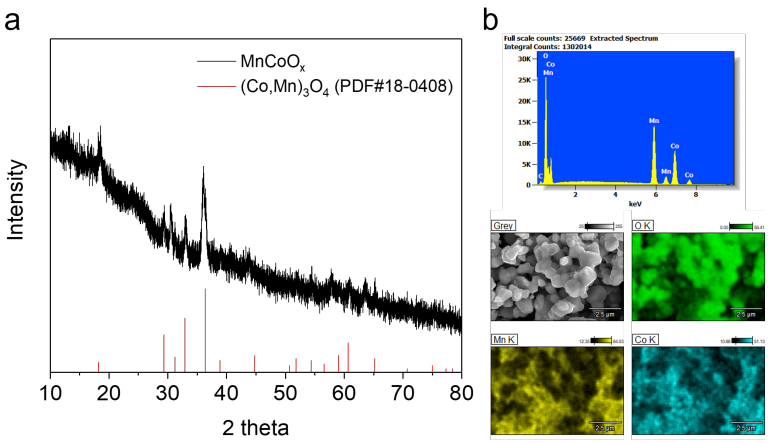

Figure S7. (a) PXRD pattern, (b) EDX spectrum and corresponding elemental mapping for $MnCoO_x$.

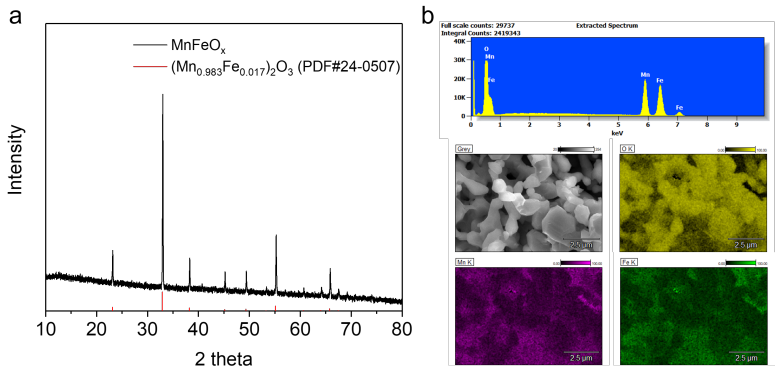

Figure S8. (a) PXRD pattern, (b) EDX spectrum and corresponding elemental mapping for $MnFeO_x$.

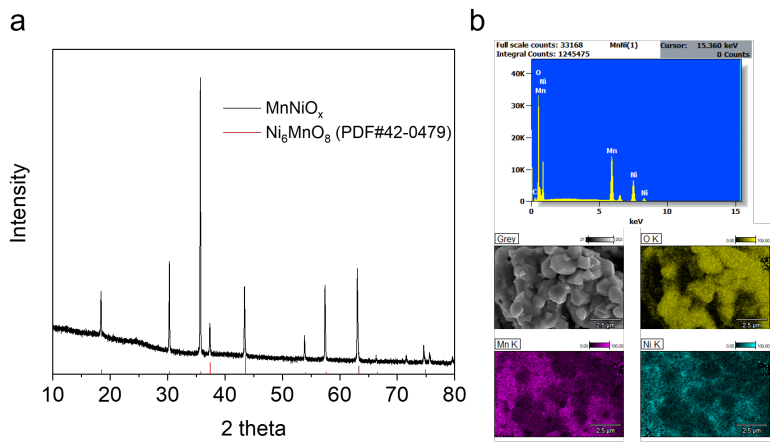

Figure S9. (a) PXRD pattern, (b) EDX spectrum and corresponding elemental mapping for MnNiO$_x$.

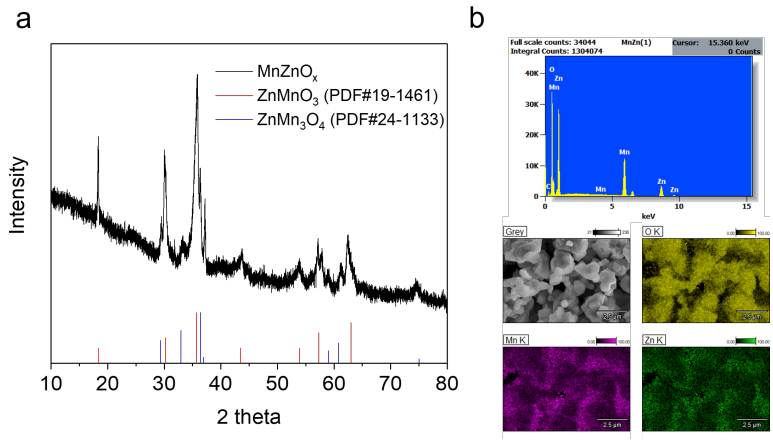

Figure S10. (a) PXRD pattern, (b) EDX spectrum and corresponding elemental mapping for MnZnO$_x$.

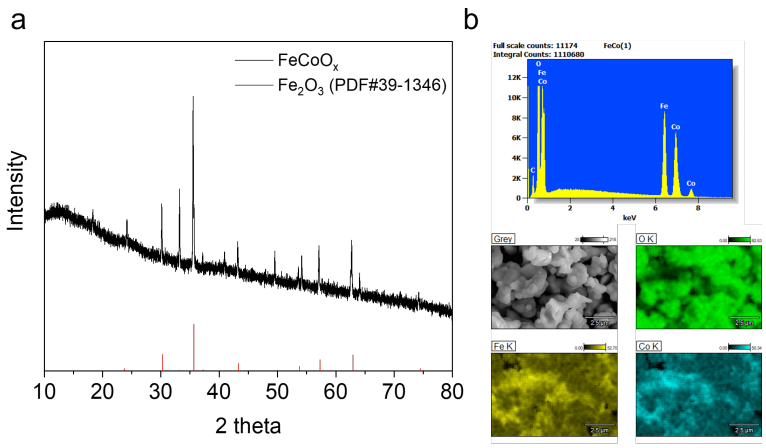

Figure S11. (a) PXRD pattern, (b) EDX spectrum and corresponding elemental mapping for FeCoO$_x$.

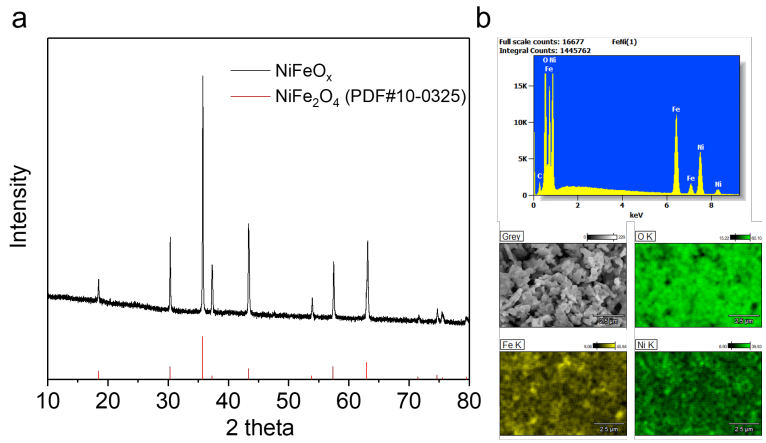

Figure S12. (a) PXRD pattern, (b) EDX spectrum and corresponding elemental mapping for FeNiO$_x$.

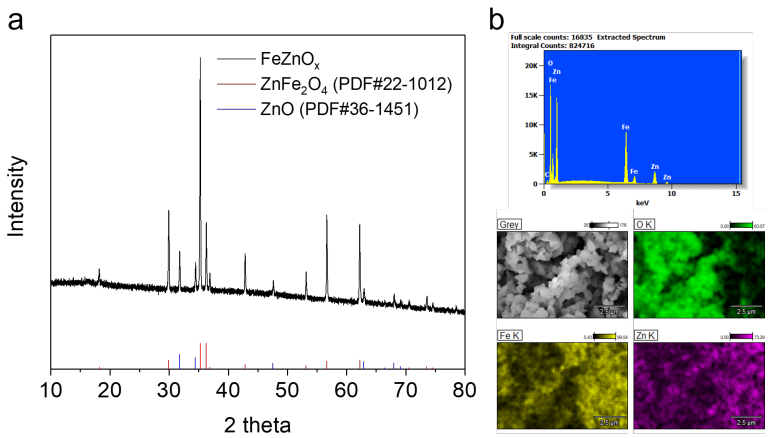

Figure S13. (a) PXRD pattern, (b) EDX spectrum and corresponding elemental mapping FeZnO$_x$.

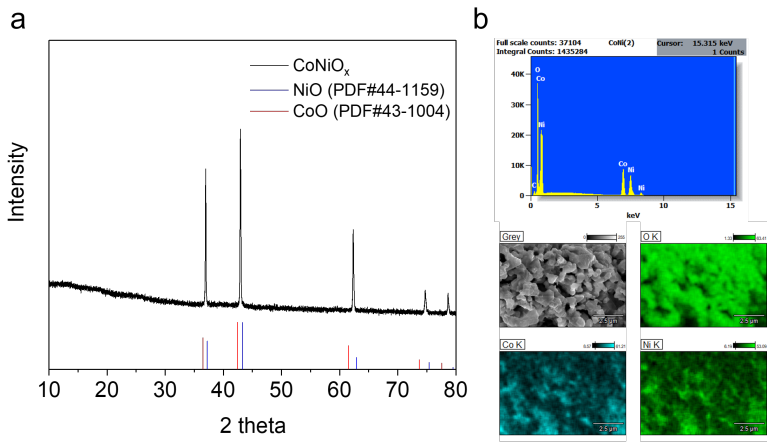

Figure S14. (a) PXRD pattern, (b) EDX spectrum and corresponding elemental mapping for CoNiO$_x$.

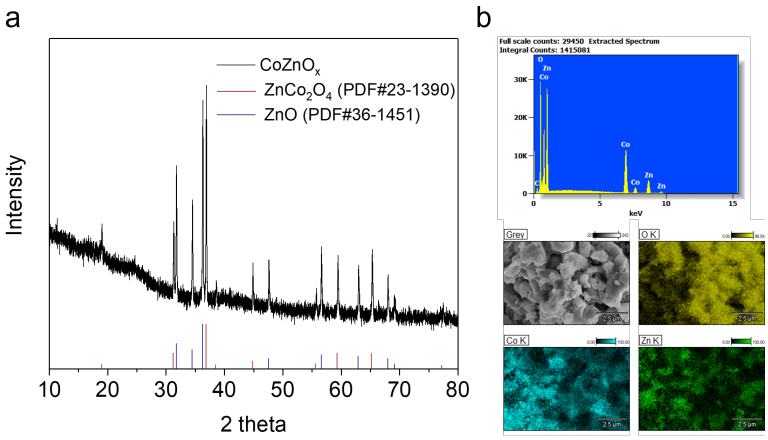

Figure S15. (a) PXRD pattern, (b) EDX spectrum and corresponding elemental mapping for $CoZnO_x$.

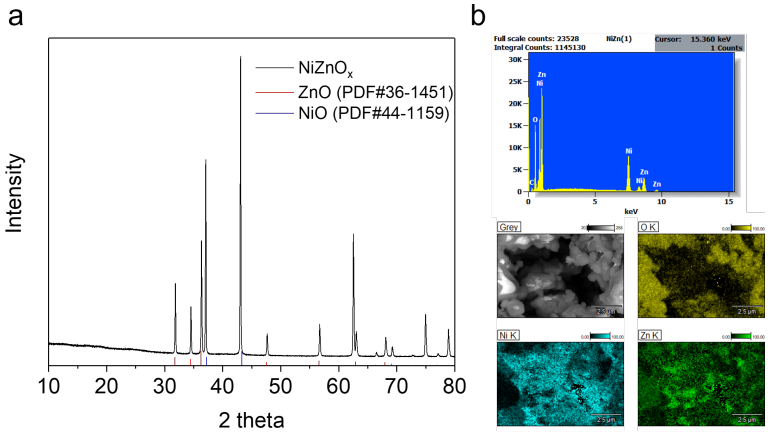

Figure S16. (a) PXRD pattern, (b) EDX spectrum and corresponding elemental mapping for $NiZnO_x$.

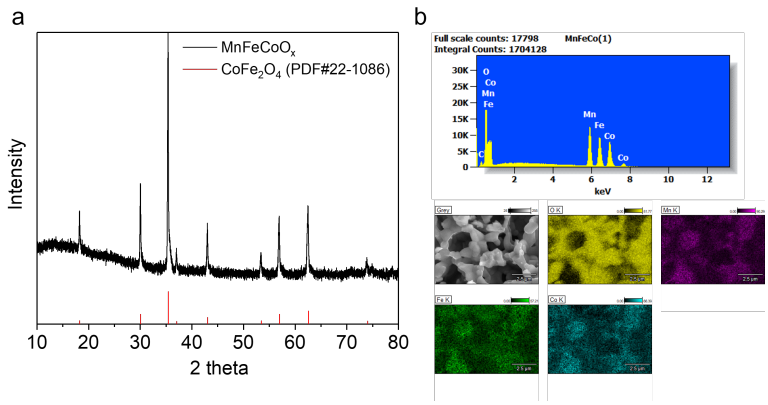

Figure S17. (a) PXRD pattern, (b) EDX spectrum and corresponding elemental mapping for $MnFeCoO_x$.

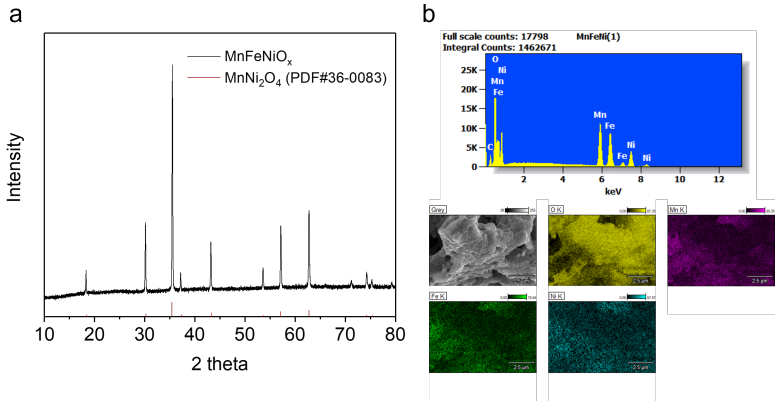

Figure S18. (a) PXRD pattern, (b) EDX spectrum and corresponding elemental mapping for MnFeNiO$_x$.

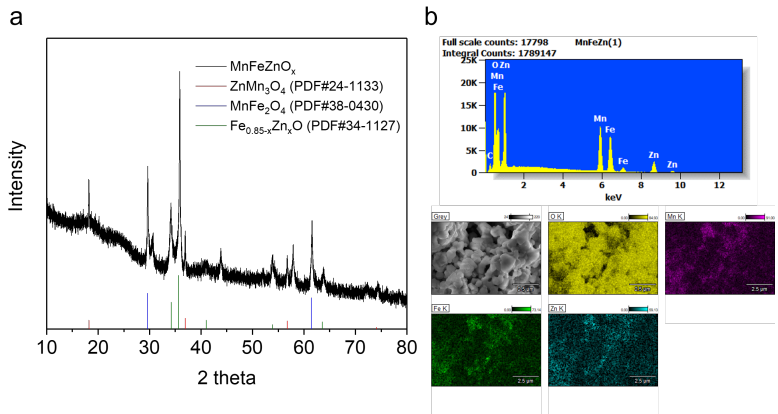

Figure S19. (a) PXRD pattern, (b) EDX spectrum and corresponding elemental mapping for MnFeZnO$_x$.

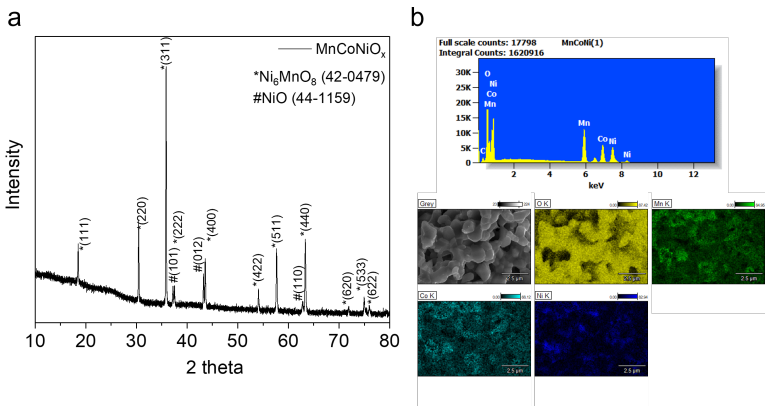

Figure S20. (a) PXRD pattern, (b) EDX spectrum and corresponding elemental mapping for MnCoNiO$_x$.

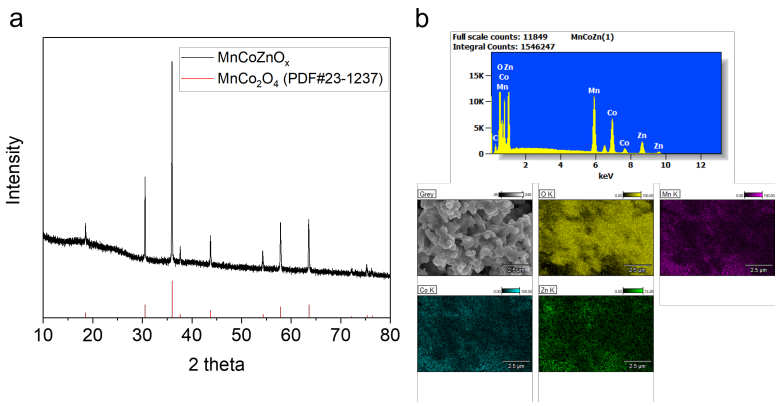

Figure S21. (a) PXRD pattern, (b) EDX spectrum and corresponding elemental mapping for $MnCoZnO_x$.

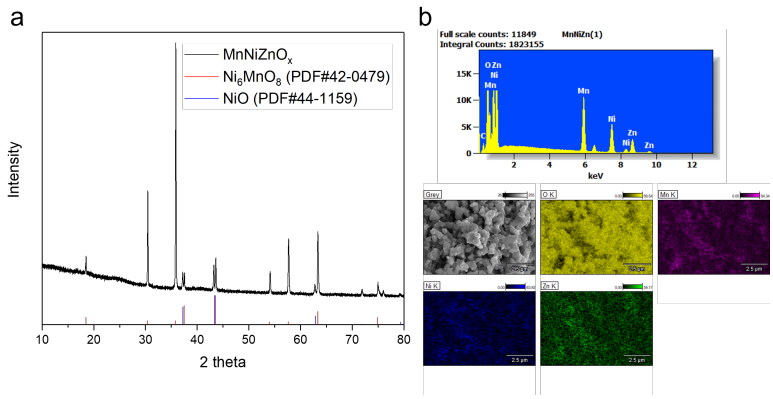

Figure S22. (a) PXRD pattern, (b) EDX spectrum and corresponding elemental mapping for $MnNiZnO_x$.

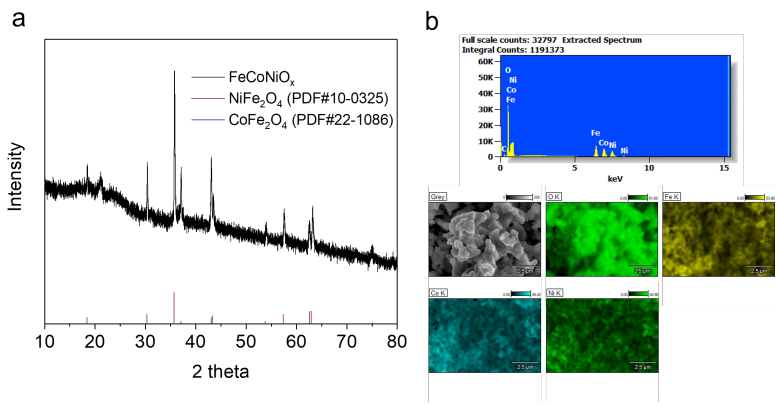

Figure S23. (a) PXRD pattern, (b) EDX spectrum and corresponding elemental mapping for $FeCoNiO_x$.

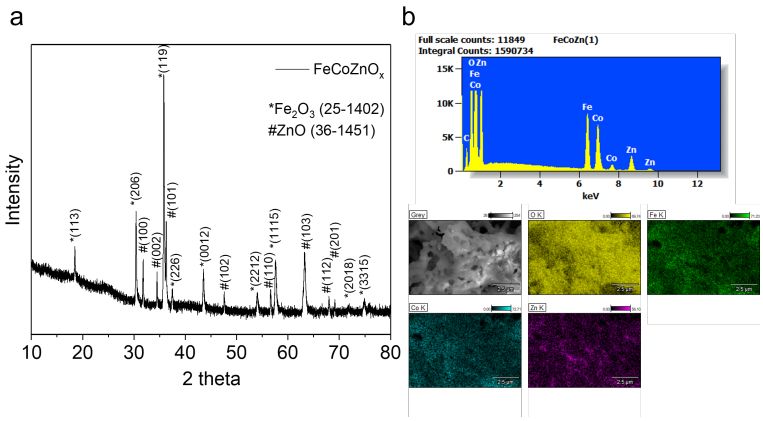

Figure S24. (a) PXRD pattern, (b) EDX spectrum and corresponding elemental mapping for FeCoZnO$_x$.

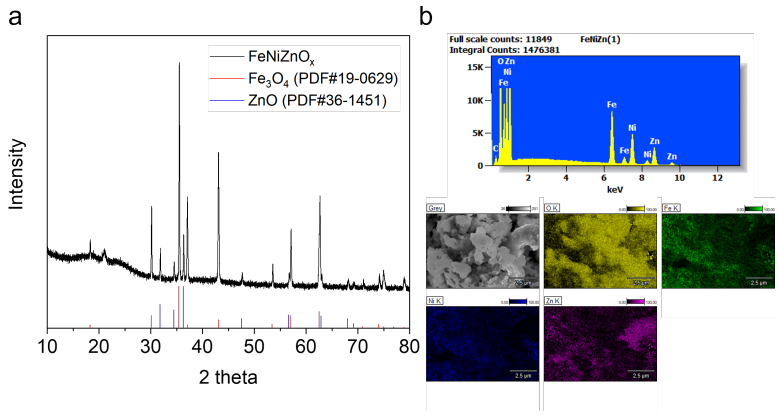

Figure S25. (a) PXRD pattern, (b) EDX spectrum and corresponding elemental mapping for FeNiZnO$_x$.

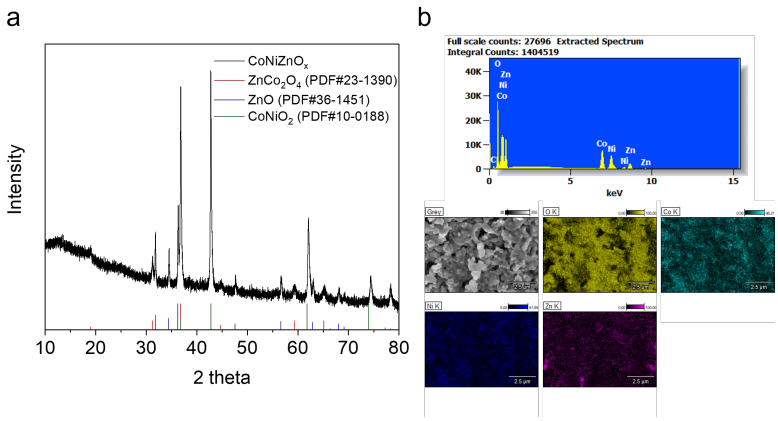

Figure S26. (a) PXRD pattern, (b) EDX spectrum and corresponding elemental mapping for CoNiZnO$_x$.

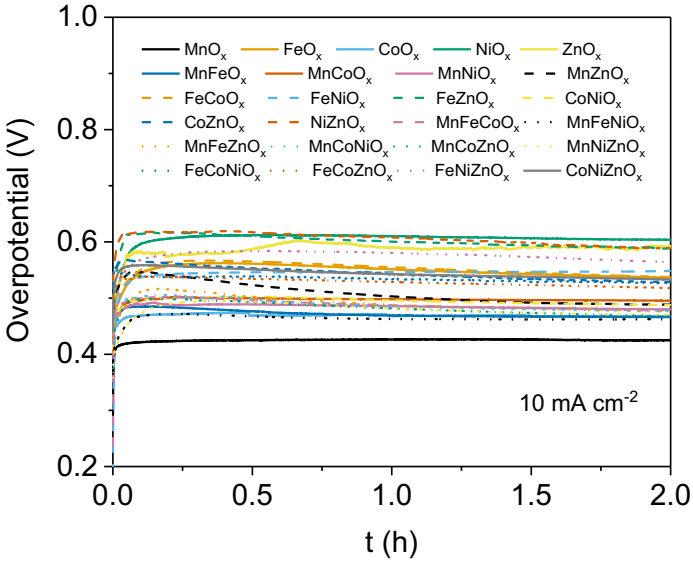

Figure S27. Stability tests of the MO_x/GPO, $MM'O_x$/GPO and $MM'M''O_x$/GPO electrodes in chronopotentiometry measurements at 10 mA cm^{-2} in 1 M H_2SO_4 electrolyte.

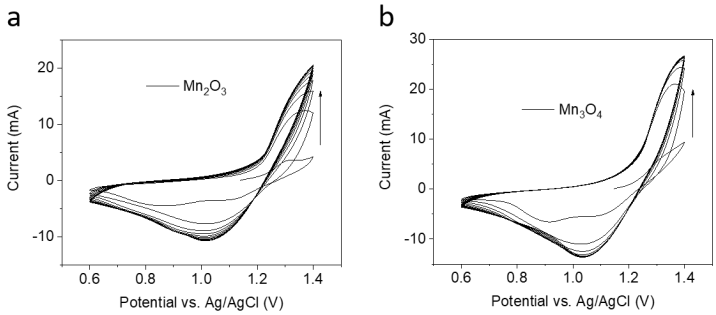

Figure S28. 10-cycle cyclic voltammograms of (a) Mn_2O_3/GPO and (b) Mn_3O_4/GPO at scan rate of 50 mV s^{-1}.

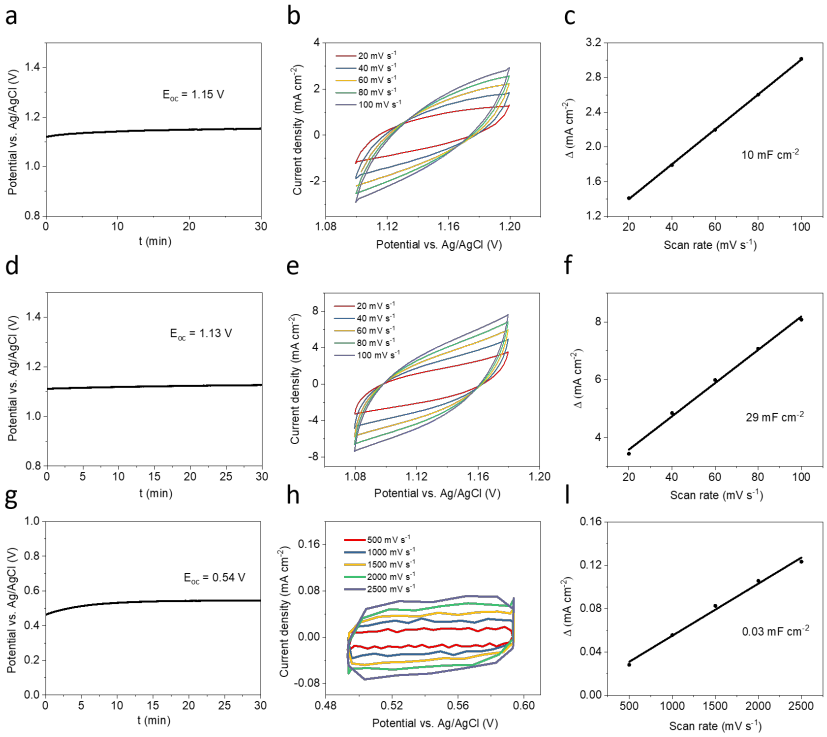

Figure S29. Electrochemical double-layer capacitance (EDLC) measurements: OCP (vs. Ag/AgCl) values recording within 30 mins of (a) Mn_3O_4/GPO, (d) Mn_2O_3/GPO and (g) GPO; CV curves under different scan rates of (b) Mn_3O_4/GPO, (e) Mn_2O_3/GPO and (h) GPO; The scan rate dependences of the current density differences Δ of (c) Mn_3O_4/GPO, (f) Mn_2O_3/GPO and (I) GPO.

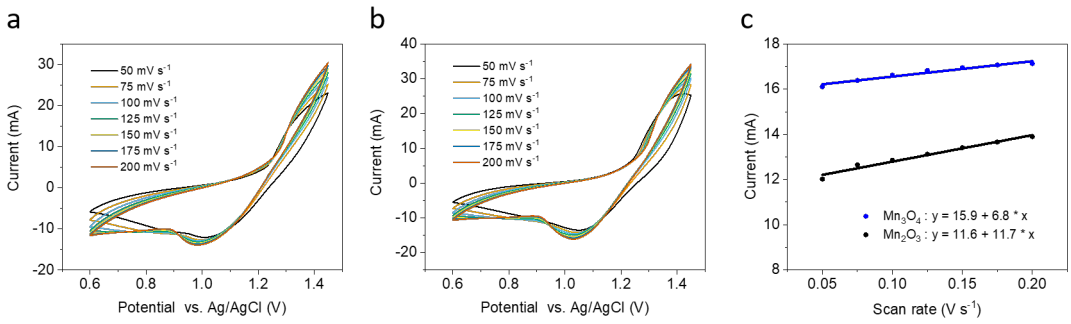

Figure S30. Cyclic voltammograms of (a) Mn_2O_3/GPO and (b) Mn_3O_4/GPO at different scan rates from 50 to 200 mV s^{-1}. (c) Linear dependence of the peak current of the Mn^{4+}/Mn^{3+} reduction wave vs. scan rate.

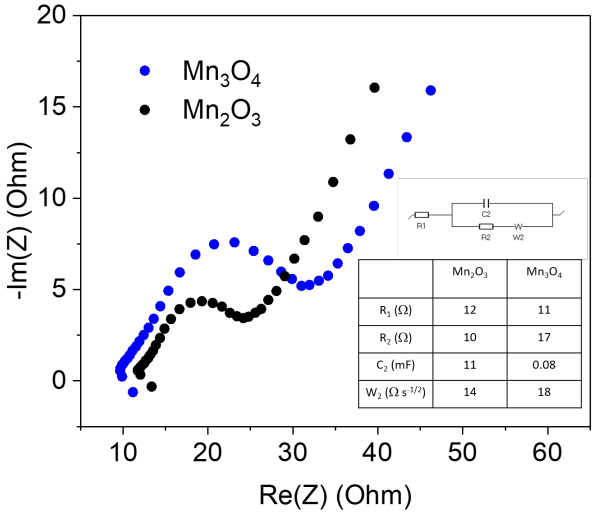

	Mn_2O_3	Mn_3O_4
R_1 (Ω)	12	11
R_2 (Ω)	10	17
C_2 (mF)	11	0.08
W_2 ($\Omega\, s^{-1/2}$)	14	18

Figure S31. EIS spectra of Mn_2O_3/GPO (black) and Mn_3O_4/GPO (blue).

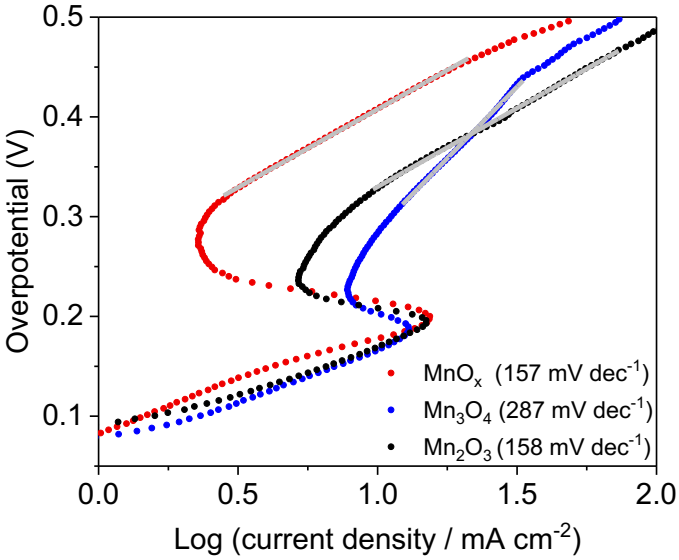

Figure S32. Tafel plots of MnO_x/GPO, Mn_2O_3/GPO and Mn_3O_4/GPO extracted from LSV data.

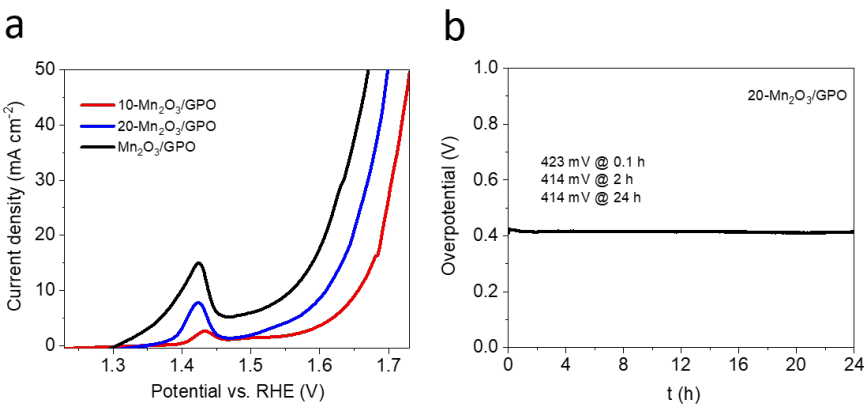

Figure S33. (a) electrocatalytic activity of Mn_2O_3/GPO, 10-Mn_2O_3/GPO and 20-Mn_2O_3/GPO; (b) stability tests of 20-Mn_2O_3/GPO in chronopotentiometry measurements at 10 mA cm^{-2} for 24 h.

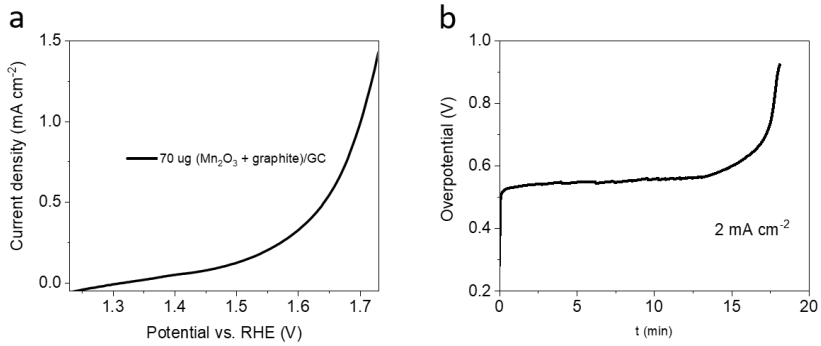

Figure S34. (a) electrocatalytic activity and (b) stability test in chronopotentiometry measurement at 2 mA cm^{-2} for of Mn_2O_3+graphite/GC.

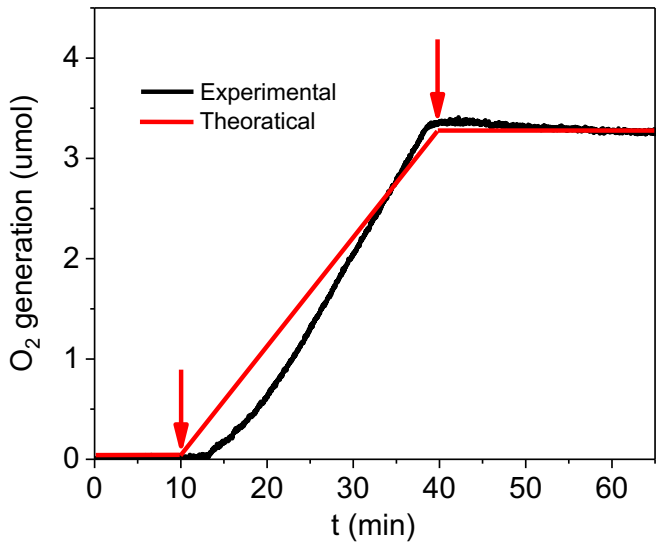

Figure S35. Time evolution of oxygen production amount in the anode headspace during a chronopotentiometry at the constant current density of 10 mA cm^{-2} for 30 minutes. The arrows indicate initial and final electrolysis times. 3 mins after the chronopotentiometry starts, the O_2 signal rapidly increases, reaching a total ~3.26 umol production of O_2 in steady state conditions. This corresponds to a >99% Faradaic efficiency.

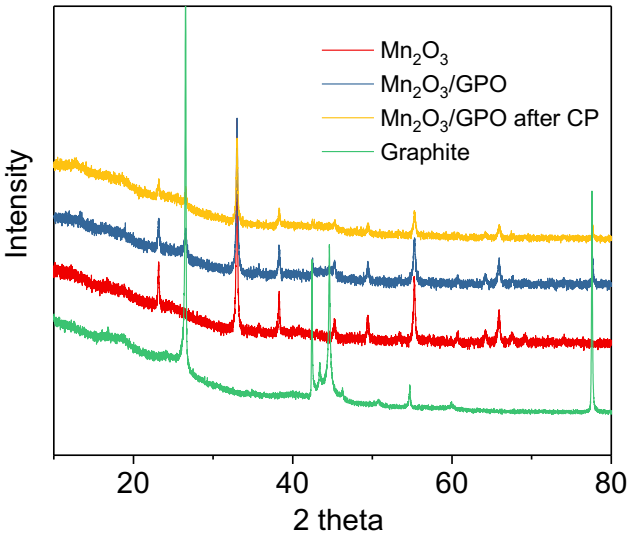

Figure S36. PXRD patterns of commercial graphite, Mn_2O_3, Mn_2O_3/GPO and Mn_2O_3/GPO after 2h catalysis (washed with acetone to remove paraffin oil)

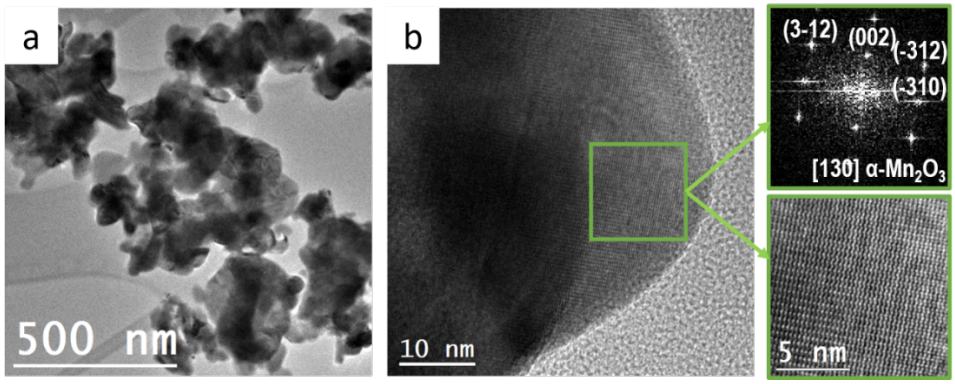

Figure S37. Low mag. TEM (a) and HRTEM (b) micrographs from as-prepared Mn_2O_3. It was found that the NPs possess orthorhombic Pcab α-Mn2O3 phase (S.G.: 61) here imaged along its [130] zone axis.

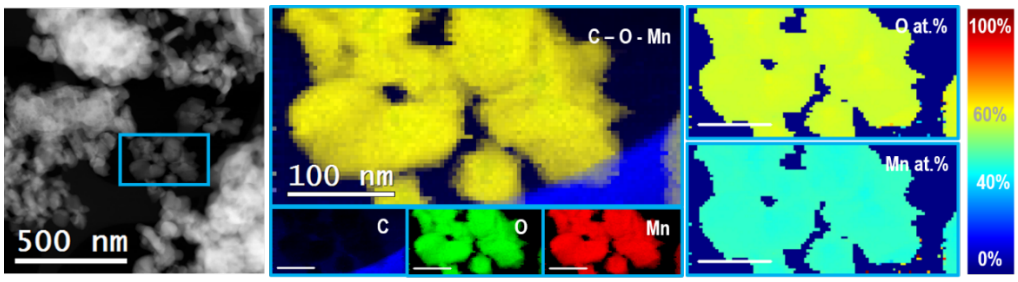

Figure S38. STEM-HAADF and STEM-EELS analysis of as-prepared Mn_2O_3 considering C K edge at 284 eV (blue), O K edge at 532 eV (green) and Mn L edge at 640 eV (red). All the Mn nanoparticles are fully oxidized, confirming the stoichiometry found from HRTEM. Carbon signal comes from the lacey carbon support with an ultrathin carbon layer supported on a Cu mesh, from Ted Pella. (All scale bars correspond to 100 nm)

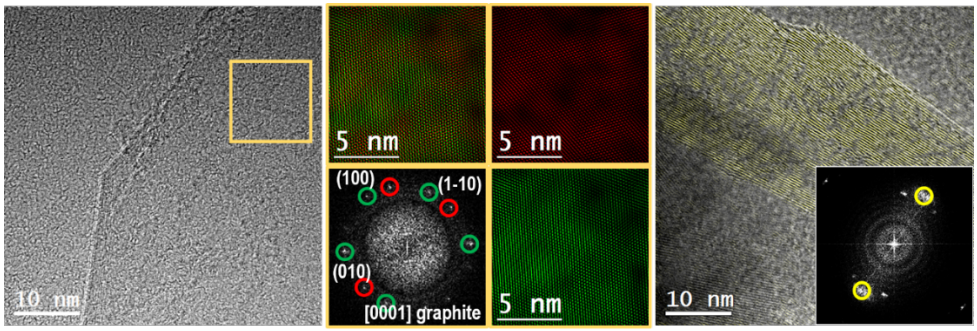

Figure S39. HRTEM analysis of Mn_2O_3/GPO. We could identify the presence of crystalline graphite, as here evidenced. In particular, from the power spectrum analysis we can distinguish two layers 22° rotated one with respect to the other, in red and green respectively. Here the structure is 2H oriented along its [0001] zone axis. In the image on the right the graphite is imaged along the side, evidencing an interplanar distance of around 3.4 nm.

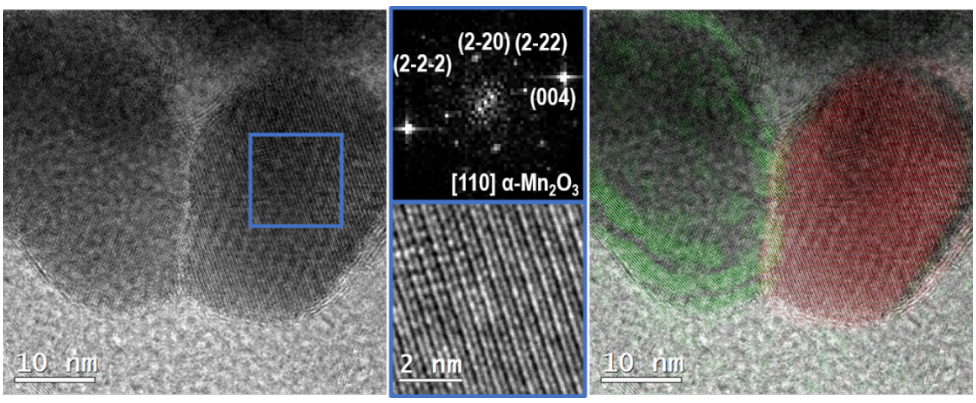

Figure S40. HRTEM analysis of Mn_2O_3/GPO. The NPs possess orthorhombic Pcab α-Mn_2O_3 atomic structure (sg 61) here imaged along its [110] zone axis. Here the presence of two nanoparticles possessing the same atomic structure is highlighted in the frequency filtered map reported on the right side in green and red, respectively.

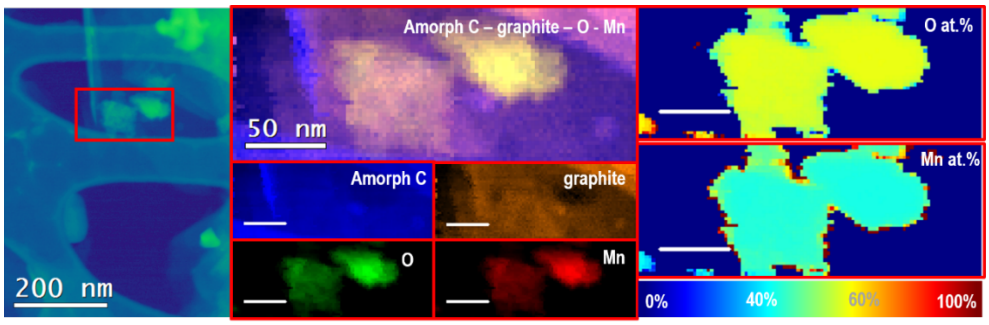

Figure S41. STEM-HAADF and STEM-EELS analysis of Mn_2O_3/GPO considering C K edge at 284 eV (blue), O K edge at 532 eV (green) and Mn L edge at 640 eV (red). We could separate the graphitic typical peak arising from C edge, from the C amorphous from the TEM grid support. All the Mn nanoparticles are fully oxidized, confirming the stoichiometry evaluated in HRTEM (all scale bars correspond to 50 nm).

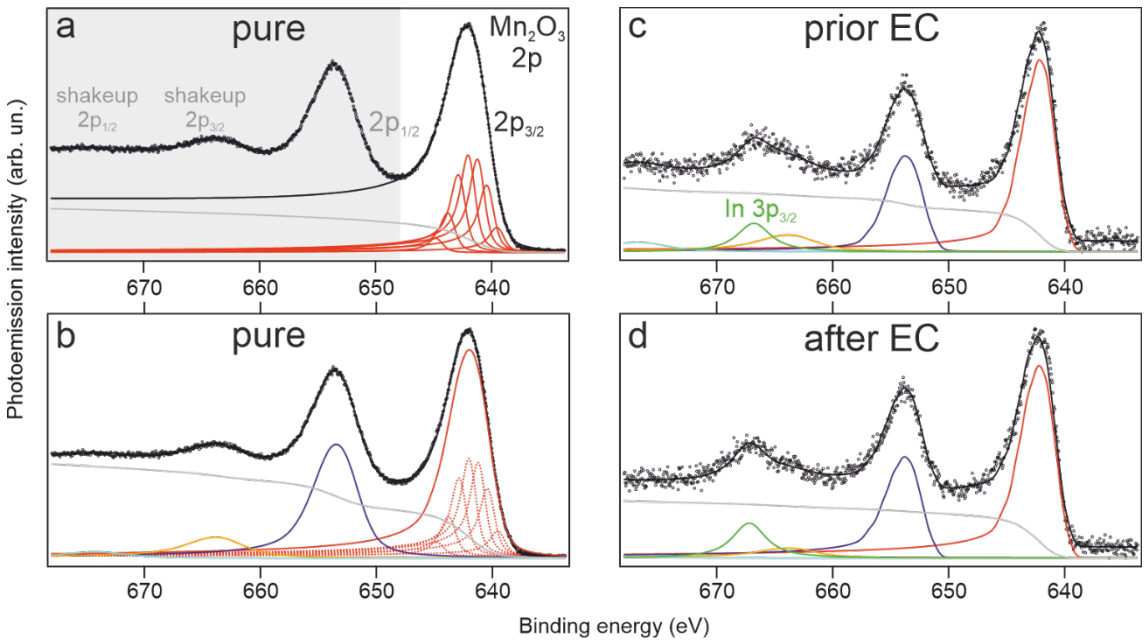

Figure S42. Mn 2p core level fit of XPS: (a) Mn $2p_{3/2}$ core level fit with seven Doniach- Šunjic lines[12] (red) and a Shirley background[13] (grey) of pure Mn_2O_3 powder. The $2p_{1/2}$ and shakeups (grey background) emissions were excluded from the fit. (b) Complete Mn 2p core level fit of Mn_2O_3 powder with four septuplets formed from the seven peaks extracted from the fit of the Mn $2p_{3/2}$. (c), (d) Mn 2p core level fit of the Mn2O3 electrode prior and after electrocatalysis using the same four septuplets as in (b), respectively. The peak-to-peak distance and core level positions are very similar to the Mn_2O_3 powder sample emissions ($\Delta E < 0.2$ eV). The emission of the In $3p_{3/2}$ from the substrate foil was taken into account by a simple Doniach- Šunjic lineshape with Shirley background.

Table S1. The metal salt precursors of syntheses, corresponding XRD phases, metal mole ratios by EDX, Ohmic drop values determined by the automatic current interrupt (CI) software and actual mass of catalysts in working electrodes of different oxides.

Oxide	Precursor (mole ratio)	XRD phase	Metal mole ratio by EDX	Ohmic drop (Ω)	Total mass in the electrode (mg)
MnO_x	$Mn(NO_3)_2{\cdot}4H_2O$	Mn_2O_3, Mn_3O_4		11	41
Mn_2O_3	-	Mn_2O_3		9	38
Mn_3O_4	-	Mn_3O_4		8	40
FeO_x	$Fe(NO_3)_3{\cdot}9H_2O$	Fe_2O_3		16	39
CoO_x	$Co(NO_3)_2{\cdot}6H_2O$	Co_3O_4		18	42
NiO_x	$Ni(NO_3)_2{\cdot}6H_2O$	NiO		15	47
ZnO_x	$Zn(NO_3)_2{\cdot}6H_2O$	ZnO		16	42
$MnFeO_x$	$Mn(NO_3)_2{\cdot}4H_2O$/ $Fe(NO_3)_3{\cdot}9H_2O$ (1:1)	$(Mn, Fe)_2O_3$	Mn/Fe: 26/25	10	41
$MnCoO_x$	$Mn(NO_3)_2{\cdot}4H_2O$/$Co(NO_3)_2{\cdot}6H_2O$ (1:1)	$(Co, Mn)_3O_4$	Mn/Co: 10/9	12	43
$MnNiO_x$	$Mn(NO_3)_2{\cdot}4H_2O$/ $Ni(NO_3)_2{\cdot}6H_2O$ (1:1)	Ni_6MnO_8	Mn/Ni: 28/27	9	44

$MnZnO_x$	$Mn(NO_3)_2{\cdot}4H_2O$/ $Zn(NO_3)_2{\cdot}6H_2O$ (1:1)	$ZnMnO_3$, $ZnMn_3O_4$	Mn/Zn: 13/11	11	41
$FeCoO_x$	$Fe(NO_3)_3{\cdot}9H_2O$/$Co(NO_3)_2{\cdot}6H_2O$ (1:1)	Fe_2O_3	Fe/Co: 25/22	13	45
$FeNiO_x$	$Fe(NO_3)_3{\cdot}9H_2O$/$Ni(NO_3)_2{\cdot}6H_2O$ (1:1)	$NiFe_2O_4$	Fe/Ni: 11/10	19	43
$FeZnO_x$	$Fe(NO_3)_3{\cdot}9H_2O$/$Zn(NO_3)_2{\cdot}6H_2O$ (1:1)	$ZnFe_2O_4$, ZnO	Fe/Zn: 33/23	7	44
$CoNiO_x$	$Co(NO_3)_2{\cdot}6H_2O$ / $Ni(NO_3)_2{\cdot}6H_2O$ (1:1)	CoO/NiO	Co/Ni: 25/23	14	44
$CoZnO_x$	$Co(NO_3)_2{\cdot}6H_2O$ / $Zn(NO_3)_2{\cdot}6H_2O$ (1:1)	$ZnCo_2O_4$, ZnO	Co/Zn: 31/22	10	41
$NiZnO_x$	$Ni(NO_3)_2{\cdot}6H_2O$ / $Zn(NO_3)_2{\cdot}6H_2O$ (1:1)	NiO, ZnO	Ni/Zn: 37/27	9	45
$MnFeCoO_x$	$Mn(NO_3)_2{\cdot}4H_2O$/$Fe(NO_3)_3{\cdot}9H_2O$/$Co(NO_3)_2{\cdot}6H_2O$ (1:1:1)	$CoFe_2O_4$	Mn/Fe/Co: 18/15/17	18	38
$MnFeNiO_x$	$Mn(NO_3)_2{\cdot}4H_2O$/$Fe(NO_3)_3{\cdot}9H_2O$/$Ni(NO_3)_2{\cdot}6H_2O$ (1:1:1)	$NiFe_2O_4$, $MnNi_2O_4$	Mn/Fe/Ni: 21/17/14	9	40
$MnFeZnO_x$	$Mn(NO_3)_2{\cdot}4H_2O$/$Fe(NO_3)_3{\cdot}9H_2O$/$Zn(NO_3)_2{\cdot}6H_2O$ (1:1:1)	$ZnMn_3O_4$, $(Fe, Zn)_{0.85}O$, $MnFe_2O_4$	Mn/Fe/Zn: 16/13/12	11	40
$MnCoNiO_x$	$Mn(NO_3)_2{\cdot}4H_2O$/$Co(NO_3)_2{\cdot}6H_2O$/$Ni(NO_3)_2{\cdot}6H_2O$ (1:1:1)	NiO, Ni_6MnO_8	Mn/Co/Ni: 16/14/15	15	39
$MnCoZnO_x$	$Mn(NO_3)_2{\cdot}4H_2O$/$Co(NO_3)_2{\cdot}6H_2O$/$Zn(NO_3)_2{\cdot}6H_2O$ (1:1:1)	$MnCo_2O_4$	Mn/Co/Zn: 17/16/13	10	42
$MnNiZnO_x$	$Mn(NO_3)_2{\cdot}4H_2O$/$Ni(NO_3)_2{\cdot}6H_2O$/$Zn(NO_3)_2{\cdot}6H_2O$ (1:1:1)	Ni_6MnO_8, NiO	Mn/Ni/Zn: 8/8/7	8	44
$FeCoNiO_x$	$Fe(NO_3)_3{\cdot}9H_2O$/$Co(NO_3)_2{\cdot}6H_2O$/$Ni(NO_3)_2{\cdot}6H_2O$ (1:1:1)	$NiFe_2O_4$, $CoFe_2O_4$	Fe/Co/Ni: 17/16/16	10	44
$FeCoZnO_x$	$Fe(NO_3)_3{\cdot}9H_2O$/$Co(NO_3)_2{\cdot}6H_2O$/$Zn(NO_3)_2{\cdot}6H_2O$ (1:1:1)	Fe_2O_3, ZnO	Fe/Co/Zn: 17/16/12	26	41
$FeNiZnO_x$	$Fe(NO_3)_3{\cdot}9H_2O$/$Ni(NO_3)_2{\cdot}6H_2O$/$Zn(NO_3)_2{\cdot}6H_2O$ (1:1:1)	Fe_3O_4, ZnO	Fe/Ni/Zn: 17/16/17	8	45
$CoNiZnO_x$	$Co(NO_3)_2{\cdot}6H_2O$/$Ni(NO_3)_2{\cdot}6H_2O$/$Zn(NO_3)_2{\cdot}6H_2O$ (1:1:1)	$CoNiO_2$, $ZnCo_2O_4$, ZnO	Co/Ni/Zn: 22/19/14	9	44

Table S2. Electrocatalytic performance comparison of different Mn-based materials towards OER under acidic media.

Catalyst	$[H_2SO_4]$	Scan rate (mV s^{-1})	η (mV)[a]	Tafel slope (mV dec^{-1})	Stability	Loading (mg cm^{-2})	Ref.
Mn_2O_3 /GPO	1 M	1	328	158	24 h[a]	19	This work
MnO_2	0.1 M	1	428	80	8000 h[a]	36	1
$Ni_{0.5}Mn_{0.5}Sb_{1.7}O_x$	1 M	10	672	60	168 h[a]	~0.18	2
$Mn_xSb_{1-x}O_z$	1 M	20	508	75	2 h[a]	~	3
Ti-MnO_2	0.05 M	5	~540[b]	170	2 h @ 1.9 V	~	4
Co_2MnO_4/FTO	1 M	10	395	79.6±1.2	320 h[c]	10	5
FeMn	1 M	~	1090	~	2 h[a]	~	6
$CoMnO_x$	Pi (pH 2.5)	~	~	85	12 h[d]	~	7
$Cu_{1.5}Mn_{1.5}O_4$-800[e]	1 M	10	352	69	20 h @ 1.55 V	~	8
$Mn_{0.8}Nb_{0.2}O_2$:10F[e]	1 M	10	680	371	~90000 s @ 1.9 V	~	9
MnO_x	Pi (pH 1-3.5)	~	~	653 ± 166	~	~	10
$Cu_{1.5}Mn_{1.5}O_4$-10F[e]	0.5 M	5	>330	123	24 h[f]	1	11

[a] @10 mA cm^{-2}; [b] @2 mA cm^{-2}; [c] @ 100 mA cm^{-2}; [d] @ 0.1 mA cm^{-2}; [e] @ 40 °C; [f] @ 16 mA cm^{-2}

Table S3. Elemental analysis (ICP-MS) of manganese before and after 2 h electrocatalytic water oxidation at a constant current density of 10 mA cm^{-2} in 1 M H_2SO_4 of 40 mL.

	Mn amount (μg/L)
1 M H_2SO_4 before	–
1 M H_2SO_4 after	102

References

1. A. Li, H. Ooka, N. Bonnet, T. Hayashi, Y. Sun, Q. Jiang, C. Li, H. Han and R. Nakamura, *Angew. Chemie - Int. Ed.*, 2019, **58**, 5054–5058.

2. I. A. Moreno-Hernandez, C. A. Macfarland, C. G. Read, K. M. Papadantonakis, B. S. Brunschwig and N. S. Lewis, *Energy Environ. Sci.*, 2017, **10**, 2103–2108.

3. L. Zhou, A. Shinde, J. H. Montoya, A. Singh, S. Gul, J. Yano, Y. Ye, E. J. Crumlin, M. H. Richter, J. K. Cooper, H. S. Stein, J. A. Haber, K. A. Persson and J. M. Gregoire, *ACS Catal.*, 2018, **8**, 10938–10948.

4. R. Frydendal, E. A. Paoli, I. Chorkendorff, J. Rossmeisl and I. E. L. Stephens, *Adv. Energy Mater.*, 2015, **5**, 1500991.

5. A. Li, S. Kong, C. Guo, H. Ooka, K. Adachi, D. Hashizume, Q. Jiang, H. Han, J. Xiao and R. Nakamura, *Nat. Catal.*, 2022, **5**, 109–118.

6. C. C. L. McCrory, S. Jung, I. M. Ferrer, S. M. Chatman, J. C. Peters and T. F. Jaramillo, *J. Am. Chem. Soc.*, 2015, **137**, 4347–4357.

7. M. Huynh, T. Ozel, C. Liu, E. C. Lau and D. G. Nocera, *Chem. Sci.*, 2017, **8**, 4779–4794.

8. S. D. Ghadge, M. K. Datta, O. I. Velikokhatnyi, R. Kuruba, P. M. Shanthi and P. N. Kumta, *J. Electrochem. Soc.*, 2020, **167**, 144511.

9. S. D. Ghadge, O. I. Velikokhatnyi, M. K. Datta, P. M. Shanthi, S. Tan and P. N. Kumta, *ACS Appl. Energy Mater.*, 2020, **3**, 541–557.

10. M. Huynh, D. K. Bediako and D. G. Nocera, *J. Am. Chem. Soc.*, 2014, **136**, 6002–6010.

11. P. P. Patel, M. K. Datta, O. I. Velikokhatnyi, R. Kuruba, K. Damodaran, P. Jampani, B. Gattu, P. M. Shanthi, S. S. Damle and P. N. Kumta, *Sci. Rep.*, 2016, **6**, 1–14.

12. S. Doniach and M. Šunjic, *J. Phys. C: Solid State Physics* 1970, **3**, 285.

13. D. A. Shirley, *Phys. Rev. B* 1972, **5**, 4709.